catalysts

MDPI

Article

Steering Charge Directional Separation in MXenes/Titanium Dioxide for Efficient Photocatalytic Nitrogen Fixation

Nianhua Liu, Rong Tang, Kai Li, Bin Wang, Junze Zhao, Qing Xu, Mengxia Ji * and Jiexiang Xia *

Institute for Energy Research, School of Chemistry and Chemical Engineering, Jiangsu University, 301 Xuefu Road, Zhenjiang 212013, China

* Correspondence: jmx@ujs.edu.cn (M.J.); xjx@ujs.edu.cn (J.X.)

Abstract: Photocatalytic nitrogen fixation has attracted much attention because of its ability to synthesize ammonia under mild conditions. However, the ammonia yield is still greatly limited by the sluggish charge separation and extremely high N_2 dissociation energy. Herein, two-dimensional Ti_3C_2 MXene ultrathin nanosheets were introduced to construct Ti_3C_2/TiO_2 composites via electrostatic adsorption for photocatalytic nitrogen fixation. The photocatalytic activity experiments showed that after adding 0.1 wt% Ti_3C_2, the ammonia yield of the Ti_3C_2/TiO_2 composite reached 67.9 μmol L^{-1} after 120 min of light irradiation, nearly 3 times higher than that of the monomer TiO_2. XPS, DRS, LSV, and FTIR were used to explore the possible photocatalytic nitrogen fixation mechanism. Studies showed that a close interfacial contact has been formed via the bonding mode of =C-O between the Ti_3C_2 and TiO_2 samples. The formed =C-O bond boosts an oriented photogenerated charge separation and transfer in the Ti_3C_2/TiO_2 composite. This work provides a promising idea for constructing other efficient MXene-based composite photocatalysts for artificial photosynthesis.

Keywords: titanium dioxide; ultrathin MXene; nitrogen fixation; charge separation; artificial photosynthesis

check for updates

Citation: Liu, N.; Tang, R.; Li, K.; Wang, B.; Zhao, J.; Xu, Q.; Ji, M.; Xia, J. Steering Charge Directional Separation in MXenes/Titanium Dioxide for Efficient Photocatalytic Nitrogen Fixation. *Catalysts* **2023**, *13*, 1487. https://doi.org/10.3390/catal13121487

Academic Editor: Hideyuki Katsumata

Received: 16 October 2023
Revised: 15 November 2023
Accepted: 22 November 2023
Published: 30 November 2023

Copyright: © 2023 by the authors. Licensee MDPI, Basel, Switzerland. This article is an open access article distributed under the terms and conditions of the Creative Commons Attribution (CC BY) license (https://creativecommons.org/licenses/by/4.0/).

1. Introduction

Ammonia plays a vital role in the national economy due to its foundation in the national nitrogen fertilizer industry and is an indispensable part of chemical raw materials [1–3]. Since the beginning of the last century, ammonia synthesis has been highly dependent on conventional industrial production technology and the "Haber-Bosch" process, which uses N_2 and H_2 as raw materials, and metal Fe as a catalyst [4,5]. However, it brings about huge energy consumption for the extremely harsh reaction requirements of high temperature and high pressure, simultaneously releasing massive amounts of CO_2 gas during ammonia synthesis. Therefore, seeking a mild and sustainable technology for green ammonia production becomes extremely urgent.

In 1977, Schrauzer and Guth discovered that TiO_2 semiconductor materials can be applied for ammonia production under UV light irradiation at ambient temperature and pressure [6]. Since then, photocatalytic N_2 conversion to ammonia using water and N_2 as raw materials has received widespread attention [7–9]. The core of photocatalytic N_2 fixation technology is the design and preparation of highly efficient photocatalytic materials. At present, a variety of photocatalysts have been reported for N_2 fixation, such as Ni_2P, Bi_3O_4Br, TiO_2, and so on [10,11]. Among them, titanium dioxide (TiO_2) has attracted much attention in the field of photocatalysis because of its notable structural stability and high catalytic performance. However, the band gap of TiO_2 in the range from 3.0 to 3.2 eV is too wide and not conducive to the timely separation of photogenerated charge carriers, thus restricting the photocatalytic N_2 fixation activity of TiO_2 materials [12–15]. Therefore, how to further improve the carrier separation rate to optimize the N_2 photoreduction performance of TiO_2 materials has important research value.

Transition metal carbide/nitride (MXene) materials are novel two-dimensional materials which were prepared by etching out the "A" group in the MAX phase (A: H, Al, Ga, In, Si, Ge, Sn, Pb, P, or As) [16]. In recent years, MXene has received widespread attention in the research fields of energy storage, water treatment, catalysis, and electromagnetic shielding [17,18]. Ti_3C_2 as one of the typical MXene materials has great potential applications in the photocatalytic hydrogen evolution, CO_2 reduction, and nitrogen fixation owing to its excellent metal conductivity, hydrophilicity, electrical conductivity, chemical stability, and photostability [19–21]. In addition, the terminal on the surface of Ti_3C_2 contains the abundant functional groups (-OH, -O, and -F), providing adequate active sites for the formation of a close contact interface with other semiconductors [22]. Moreover, thanks to the strong electron transfer characteristics of Ti_3C_2, a Schottky barrier could be formed between the interface of Ti_3C_2 and the other semiconductor materials, which plays a crucial role in inhibiting the recombination of photogenerated electrons and holes [23]. Zhao et al. found that a special built-in electric field was formed by combing Ti_3C_2 with MIL-100(Fe), and thus boosted the charge transfer rate and the photocatalytic nitrogen fixation activity [24]. Hence, the fabrication of novel Ti_3C_2-based composite photocatalytic systems has a good research prospect [25].

In this work, composite photocatalysts of TiO_2 nanoparticles modified Ti_3C_2 ultrathin nanosheets (Ti_3C_2/TiO_2) were synthesized via an ultrasound-assisted method for photocatalytic nitrogen fixation. The yield of ammonia over the Ti_3C_2/TiO_2 materials and pure TiO_2 was evaluated in the absence of any sacrifice. Photocatalytic activity experiments revealed that the optimum addition of ultrathin Ti_3C_2 nanosheets was 1.0 wt%, and the NH_4^+ yield of the Ti_3C_2/TiO_2-2 composite in pure water was 3.25 times that of the pure TiO_2. The results show that the =C-O bond that formed between the ultrathin Ti_3C_2 nanosheets and the TiO_2 nanoparticles induced the directional migration of interfacial charges, greatly improving the utilization efficiency of photogenerated electrons. Thereby the enhanced photocatalytic nitrogen fixation activity of the Ti_3C_2/TiO_2 composite materials was realized.

2. Results and Discussion

The Ti_3C_2/TiO_2 composite materials were synthesized via electrostatic adsorption with different Ti_3C_2 addition contents of 0.5 wt%, 1.0 wt%, and 2.0 wt%, respectively. The transmission electron microscope (TEM) technique was used to explore the morphology of TiO_2, Ti_3C_2, and Ti_3C_2/TiO_2 samples. TEM images in Figure 1a,b show that the pure TiO_2 presents a uniform nanoparticle morphology with a diameter around 25 nm, while Ti_3C_2 is a large-size ultrathin nanosheet structure. Figure 1c shows a TEM image of the as-synthesized Ti_3C_2/TiO_2-2 composite, which distinctly reveals that a strong interfacial contact has been formed between the TiO_2 nanoparticles and the Ti_3C_2 ultrathin nanosheets. The HRTEM image of Ti_3C_2/TiO_2-2 in Figure 1d further verifies this result. The lattice fringes of 0.358 and 0.364 nm correspond to the (101) crystal plane of the TiO_2 monomer [26]. A distinct boundary can be observed between the TiO_2 nanoparticles and Ti_3C_2 ultrathin nanosheets, demonstrating the successful construction of the Ti_3C_2/TiO_2-2 composite system.

To further explore the crystal structures of the obtained TiO_2 and Ti_3C_2/TiO_2-x (x = 1, 2 and 3) samples, the materials were characterized using an X-ray powder diffractometer (XRD). As can be seen in Figure 2a, the obvious characteristic peaks at 25.3°, 37.8°, 48.1°, 53.9°, and 55.1° correspond well with the (101), (004), (200), (105), and (211) crystalline faces in the anatase phase TiO_2, respectively. For the Ti_3C_2/TiO_2 composites, the crystal phases of these composites still exactly match the anatase TiO_2 after different amounts of Ti_3C_2 were introduced [27]. It can be observed in Figure S1 (in the Supplementary Materials) that the characteristic peak (101) in the Ti_3C_2/TiO_2 composites tend toward smaller diffraction angles compared to the pure TiO_2 with the increased amount of added Ti_3C_2, indicating the existence of interaction force between Ti_3C_2 and TiO_2 samples. Moreover, no other diffraction peaks belonging to Ti_3C_2 can be found in the XRD patterns of the Ti_3C_2/TiO_2 composites, which is attributed to the small amounts of Ti_3C_2 added to the composites. FT-IR spectra were collected to further verify the coexistence of Ti_3C_2 and TiO_2, and

are shown in Figure 2b. The characteristic peaks at 511 and 700 cm^{-1} in the monomer TiO_2 and Ti_3C_2/TiO_2 materials are assigned to the telescopic vibration of Ti-O-Ti [28]. A newly emerged peak at 1051 cm^{-1} can be observed in the Ti_3C_2/TiO_2 materials, and the peak intensity enhances gradually as the amount of added Ti_3C_2 increases, which belongs to the vested in tensile vibration of =C-O [29]. It could be reasonably speculated that a linkage between C and O has been established in the Ti_3C_2/TiO_2 composite after the combination of TiO_2 and Ti_3C_2. The same phenomenon also occurs in the Raman spectra of TiO_2 and Ti_3C_2/TiO_2. In Figure S2a (in the Supplementary Materials), the series of characteristic peaks at 143.8, 196.1, 397.2, 516.3, and 639.0 cm^{-1} are attributed to the E_g, E_g, B_{1g}, A_{1g}, and E_g modes of the anatase structures, respectively. Meanwhile, the strongest peak at 143.8 cm^{-1} is derived from the extended vibration of anatase, indicating the anatase crystal phase of the obtained TiO_2 [30]. In Figure S2b (in the Supplementary Materials), the characteristic peaks at 1433 and 1558 cm^{-1} are attributed to the characteristic peaks of Ti_3C_2. Simultaneously, with the increase in the added amount of Ti_3C_2, the corresponding characteristic peak intensity of Ti_3C_2 becomes more obvious. Raman spectra further demonstrate the successful construction of the Ti_3C_2/TiO_2 composite, which is consistent with the results of HRTEM, XRD, and FTIR.

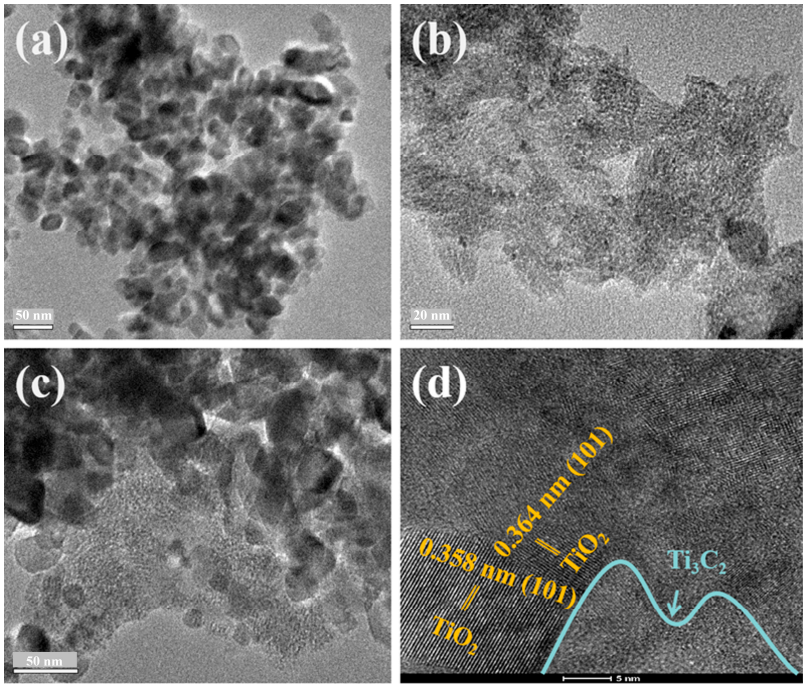


Figure 1. TEM images of the (**a**) pure TiO_2, (**b**) Ti_3C_2 ultrathin nanosheet, and (**c**) Ti_3C_2/TiO_2-2 composite material; (**d**) HRTEM image of the Ti_3C_2/TiO_2-2 composite material.

X-ray photoelectron spectroscopy (XPS) was used to investigate the elemental composition and surface chemistry of the obtained TiO_2 and Ti_3C_2/TiO_2-2 samples. In the Ti 2p high-resolution XPS spectra (Figure 3a), two peaks of 457.2 and 463.0 eV in the pure TiO_2 correspond to the Ti $2p_{3/2}$ and Ti $2p_{1/2}$ orbitals of Ti^{4+} [31]. Significantly, the Ti 2p characteristic peaks in the Ti_3C_2/TiO_2-2 shift to 457.0 and 462.8 eV in the direction of lower binding energy, illustrating that the charge density on the surface of TiO_2 has changed. It can be legitimately speculated that a charge transfer behavior occurs in the Ti_3C_2/TiO_2 composite thanks to the close contact between the TiO_2 and Ti_3C_2. In the O 1s high-resolution XPS spectra (Figure 3b), the peaks at 528.3 eV in the pure TiO_2 and 528.5 eV in Ti_3C_2/TiO_2-2 are attributed to the lattice oxygen of O-Ti-O. The peak at 530.1 eV of pure TiO_2 and at 530.1 eV of Ti_3C_2/TiO_2-2 belong to the adsorbed oxygen [32]. For the Ti_3C_2/TiO_2 composite material, the O 1s peak also shifts to the lower binding energy, which

may be caused by the mutative electron density around O atoms arising from the formation of =C-O bonds between O and C. This result is consistent with the FT-IR spectra analyses.

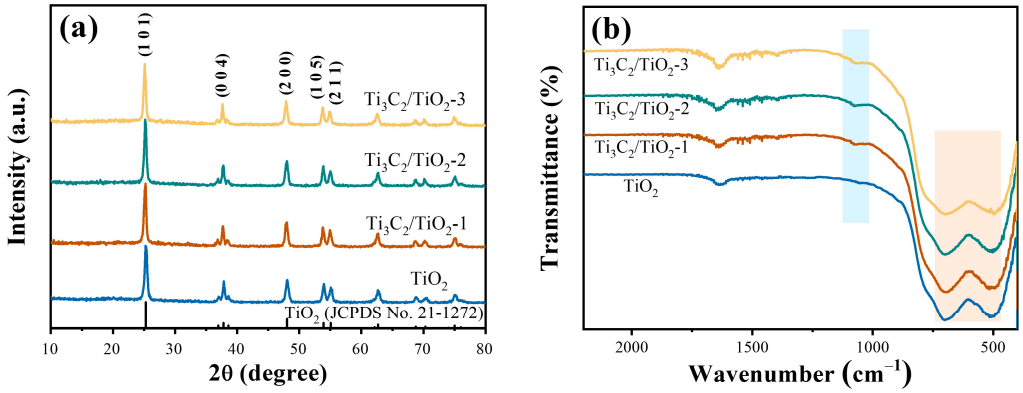


Figure 2. (**a**) XRD patterns and (**b**) FT-IR spectra of the prepared TiO_2 monomer and Ti_3C_2/TiO_2 composite materials.

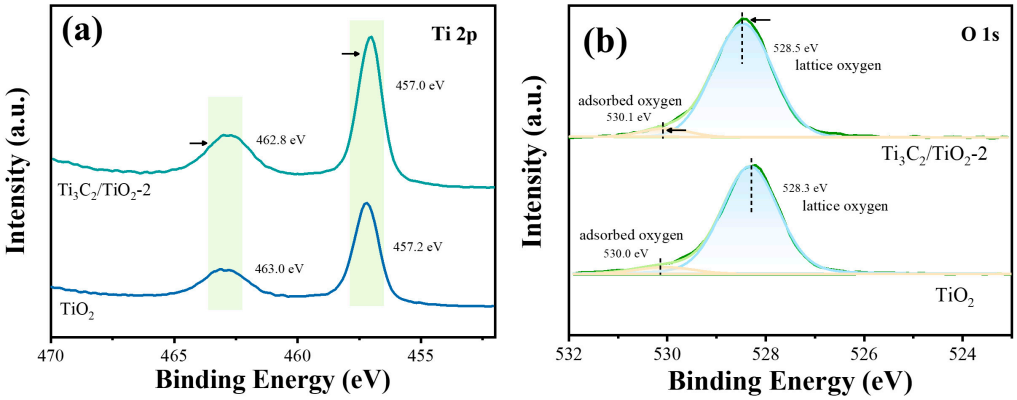


Figure 3. (**a**) Ti 2p and (**b**) O 1s XPS spectra of the pure TiO_2 and Ti_3C_2/TiO_2-2 composite material.

To delve into the effect on the photocatalytic N_2 fixation activity after the introduction of Ti_3C_2 ultrathin nanosheets, the ammonia yields of the prepared Ti_3C_2/TiO_2 composite materials and pure TiO_2 nanoparticles were systematically evaluated. Each of the photocatalytic activities were obtained from three parallel experiments. The nitrogen fixation experiments were performed under the constant temperature of 25 °C with a 300 W Xe lamp as the light source. None of the sacrifice agents or cocatalysts were introduced into the photocatalytic system throughout the process. In Figure 4, it could be found that all of the prepared materials exhibit no N_2-fixing activity in darkness. After irradiation under a Xe lamp for 120 min, the NH_4^+ yield of pure TiO_2 was determined to be 20.9 μmol L^{-1}. The photocatalytic N_2 reduction activities of the Ti_3C_2/TiO_2 composites significantly increase after the addition of different Ti_3C_2 contents. Among these samples, the Ti_3C_2/TiO_2-2 composite shows the highest NH_4^+ production performance of 67.9 μmol L^{-1}, more than thrice of that pure TiO_2. Therefore, it can be confirmed that 1.0 wt% of Ti_3C_2 is the optimal additive amount for the construction of the Ti_3C_2/TiO_2 composite photocatalytic system. The boosted N_2 photo-fixation activity in the Ti_3C_2/TiO_2 composites might be ascribable to the unique ultrathin structure of Ti_3C_2. A charge interaction via the formed =C-O linkage in the Ti_3C_2/TiO_2 composites decreases the adsorption activation of N_2, while accelerating the separation and transfer of photogenerated charge carriers. Moreover, a couple of condition experiments have been carried out, and the corresponding results are displayed in Figure S3 (in the Supplementary Materials). Activity results revealed that the production of NH_4^+ was extremely scarce without the devotion of the photocatalysts; thus, Ti_3C_2/TiO_2 is an indispensable condition for the photocatalytic N_2 reduction. Under dark conditions,

the absence of NH_4^+ production indicates that light is an indispensable driver supplying abundant electrons for the adsorption and activation of N_2. Moreover, almost no NH_4^+ can be detected after replacing N_2 with Ar, further attesting that N_2 is the source of NH_4^+ in this reaction.

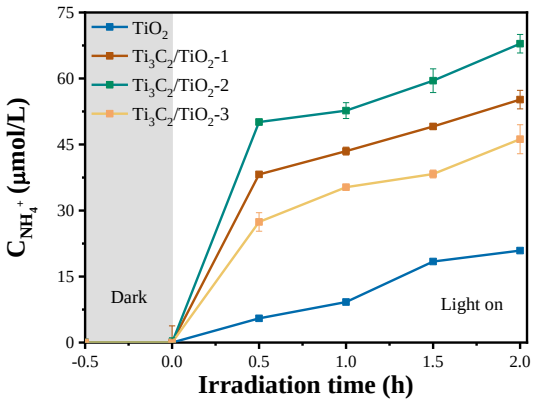


Figure 4. N_2 fixation of the pure TiO_2 and Ti_3C_2/TiO_2 composite materials.

The optical absorption properties of Ti_3C_2/TiO_2 composite materials were investigated in detail using UV-visible diffuse reflectance spectra (DRS) to reveal the role of Ti_3C_2 in the Ti_3C_2/TiO_2 composite materials (Figure 5a). The maximum absorption band edge of the monomer TiO_2 nanoparticles is estimated to be 369 nm, indicating that the TiO_2 can only be excited in the ultraviolet light region. When the amount of Ti_3C_2 is introduced, the light response range of the synthesized composite materials tend to expand to the visible light, which also proves that the construction of the composites is conducive to enhancing the visible light harvesting ability, thereby promoting the photocatalytic N_2 fixation reaction. However, it can be seen that the Ti_3C_2/TiO_2-3 composite exhibit the strongest light absorption ability among the synthesized photocatalysts. The decreased ammonia productivity of Ti_3C_2/TiO_2-3 might be caused by the diminished intrinsic absorption of the TiO_2, due to the massive Ti_3C_2 ultrathin nanosheet coating on the surface of TiO_2 nanoparticles. The N_2 adsorption–desorption isotherms shown in Figure 5b are used to explore the changes in the specific surface area of the achieved TiO_2 and Ti_3C_2/TiO_2 composite materials. According to the Brunauer–Emmett–Teller (BET) surface area data of TiO_2 and Ti_3C_2/TiO_2 composite materials, it can be observed that the surface area of the original TiO_2 was 45.96 $m^2\ g^{-1}$. The specific surface areas of Ti_3C_2/TiO_2-1, Ti_3C_2/TiO_2-2, and Ti_3C_2/TiO_2-3 composites were also determined to be 45.67, 48.46, and 48.18 $m^2\ g^{-1}$, respectively. The result shows that no significant changes have occurred in the specific surface area of the Ti_3C_2/TiO_2 composites, indicating that minimal addition of Ti_3C_2 had little effect on the specific surface area of the composite materials. BET results revealed that the specific surface area is not a crucial factor affecting photocatalytic activity.

Meanwhile, the band structure of the prepared TiO_2 nanoparticles has also been explored via different means of characterization. From the DRS measurements (Figure S4, in the Supplementary Materials), the bandgap (E_g) for the TiO_2 nanoparticles was estimated to be $\approx$ 3.05 eV [33]. Figure S5 (in the Supplementary Materials) is the valence band spectrum and the Mott–Schottky plot of the TiO_2 material. According to the Mott–Schottky plot, the intersection point of the curve and the X-axis in the figure is the flat-band potential (E_{fb}) of the TiO_2 material, which is calculated to be −0.13 V (vs. NHE) after conversion. The band gap between the valence band potential (E_{VB}), and the Fermi level of the TiO_2 material is 1.25 V, so the band gap between E_{VB} and E_{fb} is 1.25 V. Therefore, E_{VB} of the TiO_2 material can be estimated to be 1.12 V. The conduction band potential (E_{CB}) of the resulting TiO_2 material is −1.92 V according to the conduction band calculation formula $E_{CB} = E_{VB} - E_g$. According to the reduction potential of N_2 molecules, the E_{CB} of the monomer TiO_2

is sufficiently negative to drive the N_2 reduction reaction. Therefore, this photocatalytic system is feasible in thermodynamics [34,35].

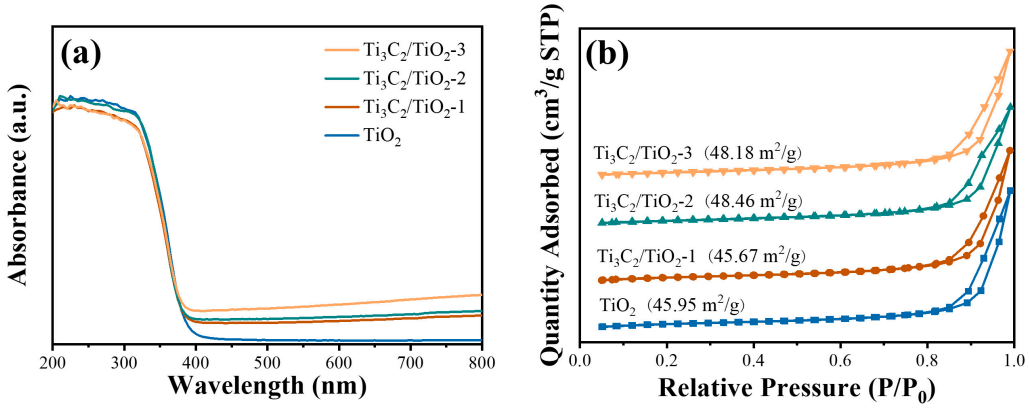


Figure 5. (**a**) UV–vis DRS spectra and (**b**) N_2 adsorption–desorption isotherms of the pure TiO_2 and Ti_3C_2/TiO_2 composite materials.

Generally, the separation and migration efficiency of photogenerated charge carriers has a decisive effect on the photocatalytic activity of semiconductors. Therefore, the charge separation behavior of the obtained photocatalysts was further studied using the photocurrent curves and electrochemical impedance spectroscopy (EIS). In Figure 6a, the transient photocurrent response tests of the prepared composite materials and pure TiO_2 were carried out under Xe lamp illumination to explore the separation of photogenerated electron–hole pairs. However, the photocurrent response value is barely detected in the pure TiO_2, indicating the low separation efficiency of the photogenerated carriers. The current values of Ti_3C_2/TiO_2 composite materials dramatically increase after combining with the Ti_3C_2, among which the Ti_3C_2/TiO_2-2 composite material possesses the highest current values [36]. The apparently enhanced current signals are attributed to the formation of close contact between Ti_3C_2 and TiO_2, advancing the separation rate of the photogenerated electrons [37]. However, a sudden decrease in the photocurrent value occurs in the Ti_3C_2/TiO_2-3 composite, which is thanks to the excess Ti_3C_2 hindering the light absorption of TiO_2. EIS tests of the monomer TiO_2 and Ti_3C_2/TiO_2 composite materials were further performed to reveal the migration ability of the photogenerated carriers, and the results are shown in Figure 6b [38]. Compared with the monomer TiO_2 material, the arc radii of the Nyquist circle of Ti_3C_2/TiO_2 composite materials are significantly reduced, indicating that the migration efficiency of photogenerated carriers of Ti_3C_2/TiO_2-x composites is improved after recombination with Ti_3C_2. Among them, the Ti_3C_2/TiO_2-2 material has the smallest arc radius, demonstrating that a higher photogenerated carrier migration ability has been achieved, which is consistent with the results of the measured photocurrent curves. The linear sweep voltammogram curves (LSV) of the pure TiO_2 and Ti_3C_2/TiO_2 composite materials were used to further explore the N_2 activation ability. The working electrode in the electrochemical test is a TiO_2 or Ti_3C_2/TiO_2-2 modified ITO electrode, and the obtained results are shown in Figure 6c,d. In the saturated N_2 atmosphere, the current densities of the pure TiO_2 and Ti_3C_2/TiO_2 composite materials are -0.42 and -0.61 mA cm^{-2}, respectively. After illuminating the working electrode for 1 min, the current densities of TiO_2 and Ti_3C_2/TiO_2 composite materials increased to -0.44 and -0.64 mA cm^{-2}, respectively. With the extension of illumination time to 5 min, the current densities of TiO_2 and Ti_3C_2/TiO_2 composite materials respectively continue to increase to -0.46 and -0.68 mA cm^{-2}, indicating that more photogenerated electrons have been produced in the Ti_3C_2/TiO_2 composite to participate in the N_2 fixation reaction. Significantly, the current densities of TiO_2 and Ti_3C_2/TiO_2 materials in the Ar atmosphere are much smaller than that of the N_2 atmosphere. Meanwhile, there is no significant change to be found after light illumination. The above data show that the photogenerated electrons

generated by the constructed Ti_3C_2/TiO_2 composite materials can effectively reduce N_2, exhibiting excellent photocatalytic ammonia production activity.

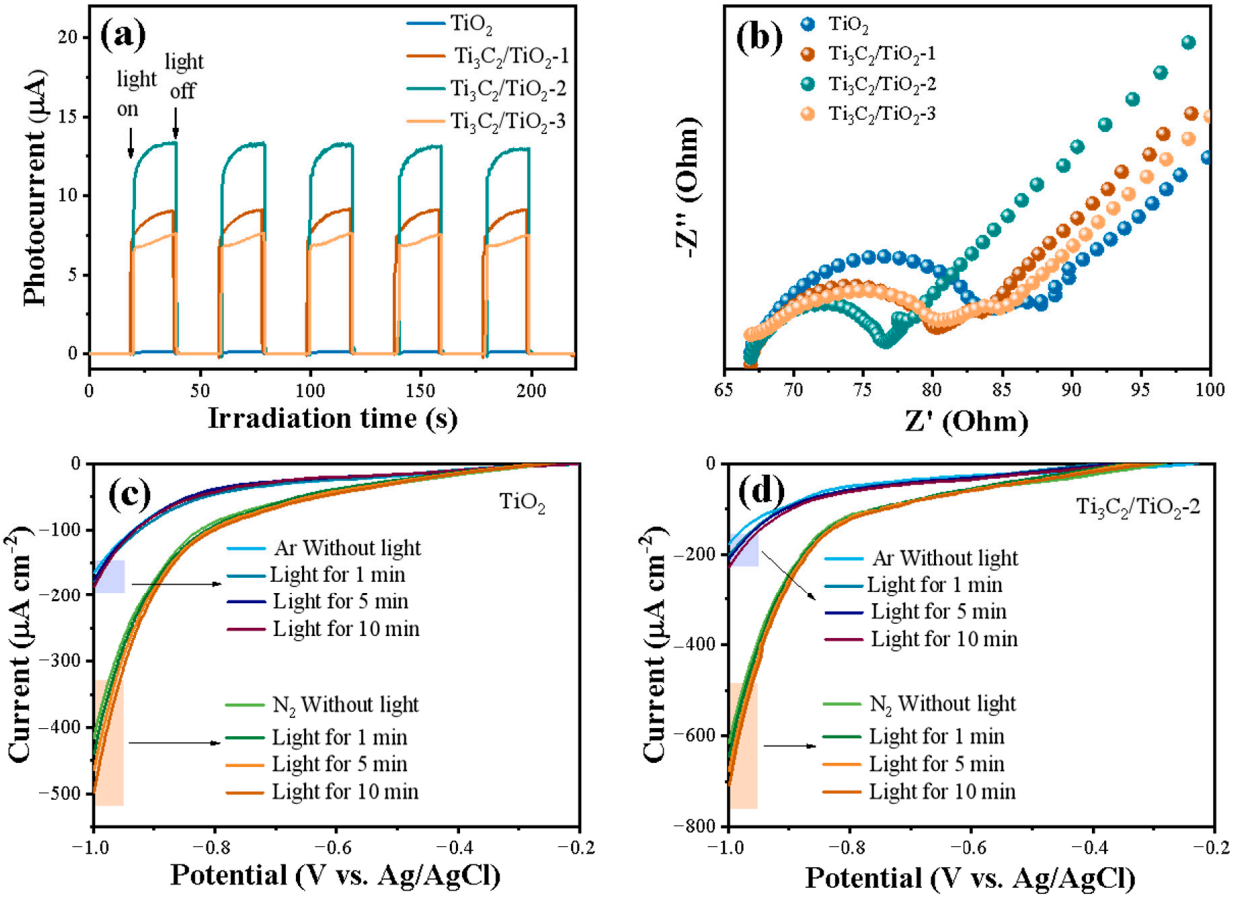


Figure 6. (**a**) Transient photocurrent response; (**b**) electrochemical impedance spectroscopy of the pure TiO_2 and Ti_3C_2/TiO_2 composite materials; Linear sweep voltammogram curves of (**c**) TiO_2 monomer and (**d**) Ti_3C_2/TiO_2-2 composite material under N_2 and Ar environments.

Based on the experimental results, a possible photocatalytic N_2 fixation mechanism for Ti_3C_2/TiO_2 was proposed (Figure 7). First of all, under illumination, the electrons located on the valence band of TiO_2 material are excited to transition to the conduction band, and Ti_3C_2 material can be used as a photogenerated electron reservoir due to its unique layered structure and the formed linkage =C-O in the Ti_3C_2/TiO_2, so that the photogenerated electrons can be further transferred to Ti_3C_2, and the photogenerated carrier recombination is inhibited, thereby effectively improving the photogenerated charge separation efficiency. In addition, Liao et al. calculated the adsorption capture capacity of TiO_2 and Ti_3C_2 materials for N_2 through DFT. The results demonstrated that the adsorption energy of Ti_3C_2 was 2.713 eV, much higher than that of TiO_2 (0.170 eV) [39]. In addition, the N=N bond lengths for the adsorbed N_2 were 1.351 Å for Ti_3C_2 and 1.113 Å for TiO_2, respectively. It could be verified that the Ti_3C_2 materials possess an excellent N_2 adsorption activation capacity. Therefore, Ti_3C_2 ultrathin nanosheets in the Ti_3C_2/TiO_2 composites could be used as active sites for adsorbing a large amount of N_2 and transforming it into an active state during the photocatalytic nitrogen fixation reaction. The photogenerated electrons enriched on the surface of Ti_3C_2 materials have a sufficient negative reduction potential to effectively reduce the adsorbed N_2 to ammonia. This work provides new ideas for the preparation of MXene-based materials.

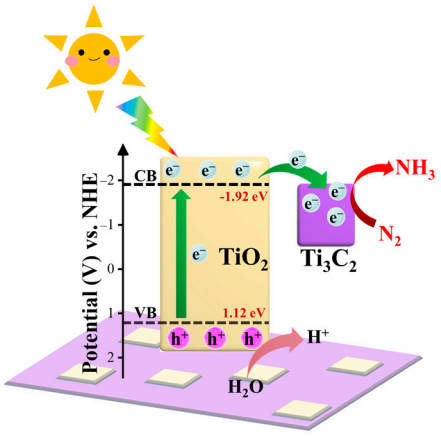


Figure 7. Ti_3C_2/TiO_2 composite materials photocatalytic nitrogen fixation mechanism. VB: valence band, CB: conduction band.

3. Materials and Methods

3.1. Materials and Characterizations

Ti_3AlC_2 of 98% purity was obtained from Forsman; hydrofluoric acid (HF), dimethyl sulfoxide (DMSO), tetrabutyl titanate, ethanol and ammonia were all fractional pure concentrations obtained from Sinopharm Chemical Reagent; potassium sodium tartrate (>99%) was obtained from Sigma-Aldrich in Shanghai, China; and Knott's reagent (13.61% NaOH, 5.07% KI, 9.49% HgI_2) was obtained from of HACH.

X-ray diffraction (XRD) patterns were tested with an XRD-6100 from Shimadzu corporation (Kyoto, Japan) with a PANalytical X'Pert Pro MPD diffractometer (Almelo, The Netherlands) using an X'Celerator RTMS detector with a Cu source at 30 KV in the range of 2θ = 10–80°; the scan rate is 7°/min. Scanning electron microscopy (SEM) was performed using a JSM-7001F from HITACHI (Tokyo, Japan). Transmission electron microscopy (TEM) was performed using a JSM-2010 from JEOL (Tokyo, Japan). Diffuse reflection spectra (DRS) of the samples were conducted on a UV–2450 spectrophotometer from SHIMADZU in the range of 200–800 nm. XPS spectra were investigated using an American VG scientific K-Alpha electron spectrometer. The surface properties were characterized by X-ray photoelectron spectroscopy (XPS, VG Scientific, Waltham, MA, USA). The binding energies were calibrated with respect to the C 1s peak (284.8 eV).

3.2. Synthesis of the TiO_2 Material

Firstly, 100 mL of anhydrous ethanol and 4 mL of tetrabutyl titanate were mixed uniformly, and then 1 mL of distilled water was added to the mixture, stirred continuously for 2 h and then ripened for 12 h. The obtained product was washed with anhydrous ethanol three times and dried at 60 °C. Next, 0.4 g of the dried product was weighed and mixed with 10 mL of anhydrous ethanol, 5 mL of water, and 0.5 mL of ammonia, stirring for 0.5 h; the resulting dispersion was transferred to a high-pressure reactor, heated under the condition of 200 °C for 16 h. Subsequently, the resulting product was centrifuged and washed three times with distilled water and anhydrous ethanol, and then dried in a vacuum to obtain the TiO_2 precursor. Finally, 0.35 g of the TiO_2 precursor was weighed with a porcelain boat and calcined in a muffle furnace at 500 °C for 120 min, with a temperature increase rate of 10 °C min^{-1}.

3.3. Synthesis of the Ti_3C_2 Ultrathin Nanosheets

This sample was synthesized based on our previous work [40]. First, 2.0 g of Ti_3AlC_2 was weighed and 30 mL of 49% hydrofluoric acid solution was added to it and stirred at 50 °C for 24 h. The resulting product was centrifuged at 5000 rpm and washed with deionized water until the pH of the solution was greater than 6, and then centrifuged at 5000 rpm for 10 min to obtain product A. Subsequently, 1.0 g of product A was weighed

and added to a solution made of 5 mL dimethyl sulfoxide (DMSO). Subsequently, 1.0 g of product A was weighed and 5 mL of dimethyl sulfoxide (DMSO) was added to form a solution, which was pumped to vacuum and stirred at room temperature for 24 h. The product was centrifuged at 5000 rpm to remove the upper layer of DMSO. The upper layer of DMSO was obtained as intermediate product B. Next, 300 mL of deionized water was added to product B, Ar was passed through it as a protective gas, and the product was ultrasonicated in an ice-water bath for 6 h. Finally, the product was centrifuged at 3500 rpm for 30 min, and the precipitate was removed. The upper layer of the solution was taken, filtered, and freeze-dried in vacuo to obtain Ti_3C_2 powder. The powder was prepared into a Ti_3C_2 solution with a concentration of 1 g L^{-1} and kept as a reserve.

3.4. Synthesis of the Ti_3C_2/TiO_2 Composite Materials

An amount of 0.099 g of final TiO_2 product was weighed in a 100 mL round-bottomed flask to which 0.5 wt%, 1 wt%, and 2 wt% Ti_3C_2 solution were added and recorded as Ti_3C_2/TiO_2-1, Ti_3C_2/TiO_2-2 and Ti_3C_2/TiO_2-3, respectively. Next, 50 mL of ethylene glycol was added to the solution, and a glass stopper was coated with vacuum grease and pumped to vacuum. To the solution, 50 mL of ethylene glycol was added, and the round-bottomed flask was evacuated to vacuum after the glass stopper was coated with vacuum grease. After stirring for 30 min at room temperature and ultrasonication for 5 h, the TiO_2 and Ti_3C_2 were compounded, and the obtained products were centrifuged at high speed, washed three times each with distilled water and anhydrous ethanol, and dried under vacuum at 60 °C to obtain Ti_3C_2/TiO_2 products.

3.5. Photocatalytic N_2 Fixation Activity Experiments

First, 50 mg of the prepared photocatalytic materials was weighed and dispersed in 100 mL of ammonia-free water. Then, N_2 was continuously passed into the photocatalytic nitrogen fixation system at a rate of 60 mL min^{-1} for 30 min under dark conditions to saturate it. The temperature was maintained at 25 °C in a circulating water bath, and a 300 W Xenon lamp was used as a light source, with a distance of 12 cm from the photocatalytic vial. The light intensity of 300 W Xenon lamp in this work was determined to be 0.046 W/cm^2 using a FZ-A radiometer. Every 1 h after the light was turned on, 7 mL of reaction solution was taken from the reaction system, centrifuged, and filtered through 0.22 μm filter membrane. Then, 5 mL of the clear solution was pipetted into a cuvette, 100 μL of potassium sodium tartrate and 100 μL of Nessler's agent were added into the cuvette, and the solution was shaken and dispersed and then left to be dispersed for 10 min. Next, 3 mL of the solution was pipetted into the cuvette and measured at the absorbance of 420 nm with an ultraviolet spectrophotometer. The concentration of ammonia in the solution was obtained by referring to the standard curve that had been developed. Each set of data was tested more than three times to ensure the accuracy of the data.

3.6. Electrochemical Tests

Electrochemical tests of the prepared photocatalytic materials were carried out in a standard three-electrode system, in which the reference electrode was a saturated Ag/AgCl electrode and the counter electrode was a platinum wire electrode. The working electrode was prepared by dispersing a certain amount of photocatalytic material in a solvent and coating it on conductive glass (ITO, 0.5 × 1 cm^2). The specific preparation method was as follows: during the photocurrent and impedance test, 2 mg of the material was ultrasonically dispersed in 200 μL of ethylene glycol, and 20 μL of the dispersed solution was added dropwise onto the conductive surface of ITO and dried with infrared lamp. For the linear voltammetry and Mott–Schottky curve tests, 5 mg of material was ultrasonically dispersed in 990 μL of isopropanol solution (isopropanol/water = 3:1) and 10 μL of naphthol mixture, and 20 μL of the dispersion was applied to the conductive surface of the ITO and dried with an infrared lamp. The electrolyte for photocurrent testing was 0.1 mol L^{-1} phosphate buffer salt solution (pH = 7); the electrochemical impedance solution was 5 mmol L^{-1}

$Fe(CN)_6^{3-}$/$Fe(CN)_6^{4-}$ in 0.1 M KCl solution. The electrolyte for testing the linear voltammetric and Mott–Schottky curves was 0.2 mol L^{-1} sodium sulfate solution. A 300 W Xenon lamp (current 15 A) was used as a light source.

4. Conclusions

In summary, the Ti_3C_2/TiO_2 composite materials were successfully prepared at room temperature by introducing the Ti_3C_2 ultrathin nanosheets into the TiO_2 nanoparticles using ethylene glycol as a solvent through a simple ultrasonic reaction. Without the addition of any sacrifices, the NH_4^+ yield of the Ti_3C_2/TiO_2-2 composite was 3.25 times than greater that of the pure TiO_2. Various studies have demonstrated that the unique layered structure of the MXene ultrathin nanosheets provides a larger specific surface area and abundant exposed active sites for the high dispersion of TiO_2 nanoparticles. Moreover, the formed =C-O linkage in the Ti_3C_2/TiO_2 composites promotes the effective separation rate and directed movement of photogenerated charge carriers, thus greatly boosting the adsorption and activation of N_2 molecules. This work provides a feasible idea for the design of MXene-based composites with high performance for artificial nitrogen-fixing.

Supplementary Materials: The following supporting information can be downloaded at: https://www.mdpi.com/article/10.3390/catal13121487/s1, Figure S1: The partial enlarged XRD patterns of the pure TiO_2 and Ti_3C_2/TiO_2 composite materials; Figure S2: Raman spectra of the (a) pure TiO_2 and (b) Ti_3C_2/TiO_2 composite materials; Figure S3: Activity diagram of Ti_3C_2/TiO_2-2 photocatalytic nitrogen fixation under controlled conditions; Figure S4: The calculated band gap of catalyst sample converted using the Tauc function from DRS spectra of TiO_2; Figure S5: (a) Mott-Schottky plots and (b) valence-band XPS spectra of the pure TiO_2.

Author Contributions: Conceptualization, N.L. and M.J.; methodology, N.L., K.L. and M.J.; validation, N.L., R.T. and K.L.; formal analysis, N.L. and K.L.; resources, M.J., B.W. and J.X.; data curation, N.L., J.Z. and Q.X.; writing—original draft preparation, N.L. and R.T.; writing—review and editing, N.L. and M.J.; visualization, N.L. and M.J.; supervision, M.J.; project administration, M.J., B.W. and J.X.; funding acquisition, M.J. and J.X. All authors have read and agreed to the published version of the manuscript.

Funding: This work was financially supported by the National Natural Science Foundation of China (No. 22108108, and No. 22108106) and the China Postdoctoral Science Foundation No. 2022M721381.

Data Availability Statement: Data are contained within the article and Supplementary Materials.

Conflicts of Interest: The authors declare that they have no known competing financial interests or personal relationships that could have appeared to influence the work reported in this paper.

References

1. Jiao, F.; Xu, B. Electrochemical Ammonia Synthesis and Ammonia Fuel Cells. *Adv. Mater.* **2018**, *31*, 1805173. [CrossRef]
2. MacFarlane, D.R.; Cherepanov, P.V.; Choi, J.; Suryanto, B.H.R.; Hodgetts, R.Y.; Bakker, J.M.; Ferrero Vallana, F.M.; Simonov, A.N. A Roadmap to the Ammonia Economy. *Joule* **2020**, *4*, 1186–1205. [CrossRef]
3. Chen, G.-F.; Yuan, Y.; Jiang, H.; Ren, S.-Y.; Ding, L.-X.; Ma, L.; Wu, T.; Lu, J.; Wang, H. Electrochemical reduction of nitrate to ammonia via direct eight-electron transfer using a copper–molecular solid catalyst. *Nat. Energy* **2020**, *5*, 605–613. [CrossRef]
4. Liang, C.; Niub, H.-Y.; Guo, H.; Niu, C.-G.; Yang, Y.-Y.; Liu, H.-Y.; Tang, W.-W.; Feng, H.-P. Efficient photocatalytic nitrogen fixation to ammonia over bismuth monoxide quantum dots-modified defective ultrathin graphitic carbon nitride. *Chem. Eng. J.* **2020**, *406*, 126868. [CrossRef]
5. Shi, R.; Zhao, Y.; Waterhouse, G.I.N.; Zhang, S.; Zhang, T. Defect Engineering in Photocatalytic Nitrogen Fixation. *ACS Catal.* **2019**, *9*, 9739–9750. [CrossRef]
6. Schrauzer, G.N.; Guth, T.D. Photolysis of Water and Photoreduction of Nitrogen on Titanium Dioxide. *J. Am. Chem. Soc.* **1977**, *99*, 7189–7193. [CrossRef]
7. Yuan, J.; Yi, X.; Tang, Y.; Liu, M.; Liu, C. Efficient Photocatalytic Nitrogen Fixation: Enhanced Polarization, Activation, and Cleavage by Asymmetrical Electron Donation to N≡N Bond. *Adv. Funct. Mater.* **2020**, *30*, 1906983. [CrossRef]
8. Cao, S.; Fan, B.; Feng, Y.; Chen, H.; Jiang, F.; Wang, X. Sulfur-doped g-C_3N_4 nanosheets with carbon vacancies: General synthesis and improved activity for simulated solar-light photocatalytic nitrogen fixation. *Chem. Eng. J.* **2018**, *353*, 147–156. [CrossRef]
9. Zhang, Y.; Chen, X.; Zhang, S.; Yin, L.; Yang, Y. Defective titanium dioxide nanobamboo arrays architecture for photocatalytic nitrogen fixation up to 780 nm. *Chem. Eng. J.* **2020**, *401*, 126033. [CrossRef]

10. Di, J.; Xia, J.; Chisholm, M.F.; Zhong, J.; Chen, C.; Cao, X.; Dong, F.; Chi, Z.; Chen, H.; Weng, Y.X.; et al. Defect-Tailoring Mediated Electron-Hole Separation in Single-Unit-Cell Bi_3O_4Br Nanosheets for Boosting Photocatalytic Hydrogen Evolution and Nitrogen Fixation. *Adv. Mater.* **2019**, *31*, 1807576. [CrossRef]
11. Shen, Z.-K.; Cheng, M.; Yuan, Y.-J.; Shen, Z.-K.; Cheng, M.; Yuan, Y.-J.; Pei, L.; Zhong, J.; Guan, J.; Li, X.; et al. Identifying the role of interface chemical bonds in activating charge transfer for enhanced photocatalytic nitrogen fixation of Ni_2P-black phosphorus photocatalysts. *Appl. Catal. B Environ.* **2021**, *295*, 120274. [CrossRef]
12. Kumaravel, V.; Mathew, S.; Bartlett, J.; Pillaia, S.C. Photocatalytic hydrogen production using metal doped TiO_2: A review of recent advances. *Appl. Catal. B Environ.* **2019**, *244*, 1021–1064. [CrossRef]
13. Zhao, H.; Liang, Z.; Liu, X.; Qiu, P.; Cui, H.; Tian, J. Noble metal-like behavior of plasmonic Bi particles deposited on reduced TiO_2 microspheres for efficient full solar spectrum photocatalytic oxygen evolution. *Chin. J. Catal.* **2020**, *41*, 333–340. [CrossRef]
14. Wu, S.; Hu, H.; Lin, Y.; Zhang, J.; Hua, Y.H. Visible light photocatalytic degradation of tetracycline over TiO_2. *Chem. Eng. J.* **2020**, *382*, 122842. [CrossRef]
15. Bakhteeva, I.A.; Medvedeva, I.V.; Zhakov, S.V.; Byzov, I.V.; Filinkova, M.S.; Uimin, M.A.; Murzakaev, A.M. Magnetic separation of water suspensions containing TiO_2. *Sep. Purif. Technol.* **2021**, *269*, 118716. [CrossRef]
16. Ghidiu, M.; Lukatskaya, M.R.; Zhao, M.-Q.; Gogotsi, Y.; Barsoum, M.W. Conductive two-dimensional titanium carbide 'clay' with high volumetric capacitance. *Nature* **2014**, *516*, 78–81. [CrossRef]
17. Bao, X.; Li, H.; Wang, Z.; Tong, F.; Liu, M.; Zheng, Z.; Wang, P.; Cheng, H.; Liu, Y.; Dai, Y.; et al. TiO_2/Ti_3C_2 as an efficient photocatalyst for selective oxidation of benzyl alcohol to benzaldehyde. *Appl. Catal. B Environ.* **2021**, *286*, 119885. [CrossRef]
18. Gogotsi, Y.; Anasori, B. The Rise of MXenes. *ACS Nano* **2019**, *13*, 8491–8494. [CrossRef]
19. Wu, Y.; Yang, D.; Zhang, Y.; Jiao, S.; Tang, W.; Wang, Z.; Wu, N.; Wang, Y.; Zhong, W.; Zhang, A.; et al. Integrated unit-cell-thin MXene and Schottky electric field into piezo-photocatalyst for enhanced photocarrier separation and hydrogen evolution. *Chem. Eng. J.* **2022**, *439*, 135640. [CrossRef]
20. Chang, H.; Li, X.; Shi, L.; Zhu, Y.-R.; Yi, T.-F. Towards high-performance electrocatalysts and photocatalysts: Design and construction of MXenes-based nanocomposites for water splitting. *Chem. Eng. J.* **2021**, *421*, 129944. [CrossRef]
21. He, F.; Zhu, B.; Cheng, B.; Yu, J.; Ho, W.; Macyk, W. 2D/2D/0D $TiO_2/C_3N_4/Ti_3C_2$ MXene composite S-scheme photocatalyst with enhanced CO_2 reduction activity. *Appl. Catal. B Environ.* **2020**, *272*, 119006. [CrossRef]
22. Tang, R.; Xiong, S.; Gong, D.; Deng, Y.; Wang, Y.; Su, L.; Ding, C.; Yang, L.; Liao, C. Ti_3C_2 2D MXene: Recent Progress and Perspectives in Photocatalysis. *ACS Appl. Mater. Interfaces* **2020**, *12*, 56663–56680. [CrossRef]
23. Khazaei, M.; Ranjbar, A.; Arai, M.; Sasaki, T.; Yunoki, S. Electronic properties and applications of MXenes: A theoretical review. *J. Mater. Chem. C* **2017**, *5*, 2488–2503. [CrossRef]
24. Wang, H.; Zhao, R.; Qin, J.; Hu, H.; Fan, X.; Cao, X.; Wang, D. MIL-100(Fe)/Ti_3C_2 MXene as a Schottky Catalyst with Enhanced Photocatalytic Oxidation for Nitrogen Fixation Activities. *ACS Appl. Mater. Interfaces* **2019**, *11*, 44249–44262. [CrossRef]
25. Li, Z.; Huang, W.; Liu, J.; Lv, K.; Li, Q. Embedding CdS@Au into Ultrathin $Ti_{3-x}C_2T_y$ to Build Dual Schottky Barriers for Photocatalytic H_2 Production. *ACS Catal.* **2021**, *11*, 8510–8520. [CrossRef]
26. Atta, S.; Pennington, A.M.; Celik, F.E.; Fabris, L. TiO_2 on Gold Nanostars Enhances Photocatalytic Water Reduction in the Near Infrared Regime. *Chem* **2018**, *4*, 2140–2153. [CrossRef]
27. Tran, N.M.; Ta, Q.T.; Noh, J.S. Unusual synthesis of safflower-shaped TiO_2/Ti_3C_2 heterostructures initiated from two-dimensional Ti_3C_2 MXene. *Appl. Surf. Sci.* **2021**, *538*, 148023. [CrossRef]
28. Lu, X.; Li, S.; Guo, W.; Zhang, F.; Qu, F. covalent organic polymer-TiO_2/Ti_3C_2 heterostructure as nonenzymatic biosensor for voltammetric detection of dopamine and uric acid. *Microchim. Acta.* **2021**, *188*, 95. [CrossRef]
29. Xue, Q.; Pei, Z.; Huang, Y.; Zhu, M.; Tang, Z.; Li, H.; Huang, Y.; Li, N.; Zhang, H.; Zhi, C. Mn_3O_4 Nanoparticles on Layer-Structured Ti_3C_2 MXene towards Oxygen Reduction Reaction and Zinc-air Battery. *J Mater Chem A* **2017**, *5*, 20818–20823. [CrossRef]
30. Liu, Q.-Y.; Wang, H.-D.; Tang, R.; Cheng, Q.; Yuan, Y.-J. Rutile TiO_2 Nanoparticles with Oxygen Vacancy for Photocatalytic Nitrogen Fixation. *ACS Appl. Nano Mater.* **2021**, *4*, 8674–8679. [CrossRef]
31. Ke, T.; Shen, S.; Rajavel, K.; Yang, K.; Lin, D. In situ growth of TiO_2 nanoparticles on nitrogen-doped Ti_3C_2 with isopropyl amine toward enhanced photocatalytic activity. *J. Hazard. Mater.* **2021**, *402*, 124066. [CrossRef]
32. Ji, M.; Shao, Y.; Nkudede, E.; Liu, Z.; Sun, X.; Zhao, J.; Chen, Z.; Yin, S.; Li, H.; Xia, J. Oxygen vacancy triggering the broad-spectrum photocatalysis of bismuth oxyhalide solid solution for ciprofloxacin removal. *J. Colloid Interface Sci.* **2022**, *626*, 221–230. [CrossRef]
33. Tang, L.; Lv, Z.-Q.; Xue, Y.-C.; Xu, L.; Qiu, W.-H.; Zheng, C.-M.; Chen, W.-Q.; Wu, M.-H. MIL-53(Fe) incorporated in the lamellar BiOBr: Promoting the visible-light T catalytic capability on the degradation of rhodamine B and carbamazepine. *Chem. Eng. J.* **2019**, *374*, 975–982. [CrossRef]
34. Ji, M.; Di, J.; Zhao, J.; Chen, C.; Zhang, Y.; Liu, Z.; Li, H.; Xia, J.; He, M.; Li, H. Orientated dominating charge separation via crystal facet homojunction inserted into BiOBr for solar-driven CO_2 conversion. *J. CO_2 Util.* **2022**, *59*, 101957. [CrossRef]
35. Wang, B.; Zhu, X.; Huang, F.; Yu Quan, Y.; Liu, G.; Zhang, X.; Xiong, F.; Huang, C.; Ji, M.; Li, H.; et al. Porous edge confinement: High carrier potential and low activation energy barrier synergistically boosting the efficiency of selective photocatalytic CO_2 conversion. *Appl. Catal. B Environ.* **2023**, *325*, 122304. [CrossRef]

36. Wang, B.; Zhang, W.; Liu, G.; Chen, H.; Weng, Y.-W.; Li, H.; Chu, P.K.; Xia, J. Excited electron-rich $Bi^{(3-x)+}$ sites: A quantum well-like structure for highly-promoted selective photocatalytic CO_2 reduction performance. *Adv. Funct. Mater.* **2022**, *32*, 2202885. [CrossRef]
37. Yue, X.; Cheng, L.; Li, F.; Xiang, Q. Highly strained Bi-MOF on bismuth oxyhalide support with tailored intermediate adsorption/desorption capability for robust CO_2 photoreduction. *Angew. Chem. Int. Ed.* **2022**, *61*, e202208414. [CrossRef]
38. Dong, J.; Chen, F.; Xu, L.; Yan, P.; Qian, J.; Chen, Y.; Yang, M.; Li, H. Fabrication of sensitive photoelectrochemical aptasensor using Ag nanoparticles sensitized bismuth oxyiodide for determination of chloramphenicol. *Microchem. J.* **2022**, *178*, 107317. [CrossRef]
39. Liao, Y.; Qian, J.; Xie, G.; Han, Q.; Dang, W.; Wang, Y.; Lv, L.; Zhao, S.; Luo, L.; Zhang, W.; et al. 2D-layered Ti_3C_2 MXenes for promoted synthesis of NH_3 on P25 photocatalysts. *Appl. Catal. B Environ.* **2020**, *273*, 119054. [CrossRef]
40. Xia, J.; Yang, S.-A.; Wang, B.; Wu, P.; Popovs, I.; Li, H.; Irle, S.; Dai, S.; Zhu, H. Boosting electrosynthesis of ammonia on surface-engineered MXene Ti_3C_2. *Nano Energy* **2020**, *72*, 104681. [CrossRef]

Disclaimer/Publisher's Note: The statements, opinions and data contained in all publications are solely those of the individual author(s) and contributor(s) and not of MDPI and/or the editor(s). MDPI and/or the editor(s) disclaim responsibility for any injury to people or property resulting from any ideas, methods, instructions or products referred to in the content.